Structure-Preserving Methods for Computing Complex Band Structures of Three Dimensional Photonic Crystals

Tsung-Ming Huang[a,*], Tiexiang Li[b,*], Jia-Wei Lin[c], Wen-Wei Lin[c], Guohua Liu[b], Heng Tian[c,*]

[a] *Department of Mathematics, National Taiwan Normal University, Taipei, 116, Taiwan*
[b] *School of Mathematics, Southeast University, Nanjing 211189, People's Republic of China*
[c] *Department of Applied Mathematics, National Chiao Tung University, Hsinchu 300, Taiwan*

Abstract

This work is devoted to the numerical computation of complex band structure $\mathbf{k} = \mathbf{k}(\omega) \in \mathbb{C}^3$ for positive ω of three dimensional isotropic dispersive or non-dispersive photonic crystals from the perspective of structured quadratic eigenvalue problems (QEPs). Our basic strategy is to fix two degrees of freedom in $\mathbf{k} \in \mathbb{C}^3$ and to view the remaining one as the eigenvalue of a quadratic operator pencil derived from Maxwell's equations. Then Yee's scheme is employed to discretize $\nabla\times$ and $\mathbf{k}\times$ operators in this quadratic operator pencil. Distinct from the others' works which either ignore or directly exploit the Hamiltonian structure of the spectrum of the resulting QEP, we reformulate this QEP into an equivalent $\top$-palindromic QEP to facilitate the use of superior structure-preserving algorithms. Ultimately we rely on the structured Arnoldi algorithm, namely the G$\top$SHIRA algorithm, to compute eigenvalues of a $\top$-skew-Hamiltonian pair which are near or in $[-2, 2]$, a much narrower region than the whole positive real axis in the origin problem. Moreover, to accelerate the inner iterations of the G$\top$SHIRA algorithm, we propose the preconditioning technique, making most of the eigenmatrix, which can essentially be seen as the Kronecker product of three discrete Fourier transformation matrices, of the commutative discretized $\partial_x, \partial_y, \partial_z$ operators. The advantage of our method is discussed in detail and corroborated by several numerical results.

Keywords: dispersive permittivity, complex band structure, gyroscopic quadratic eigenvalue problem, $\top$-palindromic quadratic eigenvalue problem, G$\top$SHIRA, FFT

*Corresponding author
Email addresses: min@ntnu.edu.tw (Tsung-Ming Huang), txli@seu.edu.cn (Tiexiang Li), tianheng@nctu.edu.tw (Heng Tian)

1. Introduction

Photonic crystals (PCs) and other metamaterials have been drawing huge attention in last three decades due to their wide applications in optics and engineering. They play a pivotal role in designing fascinating optical devices and manipulating the electromagnetic waves [21]. Briefly speaking, PCs are optical media with heterogeneous refractive indices which are repeated periodically in real spaces. Especially, a three dimensional (3D) PC must belong to one of the fourteen Bravais lattices with specific lattice translation vectors $\mathbf{a}_1, \mathbf{a}_2$ and $\mathbf{a}_3$. characterized by ε and μ only. Intrinsic properties of 3D PCs, of which only the permittivity ε and permeability μ are of our concern in this article, are lattice-periodic functions. That is, ε and μ satisfy

$$\varepsilon(\mathbf{x}+\mathbf{a}_\ell)=\varepsilon(\mathbf{x}), \quad \mu(\mathbf{x}+\mathbf{a}_\ell)=\mu(\mathbf{x}), \quad \ell=1,2,3, \quad \mathbf{x}\in\mathbb{R}^3. \tag{1}$$

Moreover, ε and μ depend only on $\mathbf{x}$ for the non-dispersive PC, and they additionally depend on the frequency ω for the dispersive PC.

The electromagnetic fields in PCs are governed by the following source-free Maxwell's equations (MEQs) in the frequency domain [21],

$$\nabla\times\mathbf{E}=\imath\omega\mu\mathbf{H}, \quad \nabla\times\mathbf{H}=-\imath\omega\varepsilon\mathbf{E}, \tag{2a}$$

$$\nabla\cdot(\mu\mathbf{H})=0, \qquad \nabla\cdot(\varepsilon\mathbf{E})=0, \tag{2b}$$

where $\imath=\sqrt{-1}$ and ω is the frequency. It follows from (1) and the Bloch theorem [12] that $\mathbf{E}$ and $\mathbf{H}$ in (2) can be factorized into

$$\mathbf{E}(\mathbf{x})=\mathrm{e}^{\imath\mathbf{k}\cdot\mathbf{x}}\boldsymbol{E}_p(\mathbf{x}), \quad \mathbf{H}(\mathbf{x})=\mathrm{e}^{\imath\mathbf{k}\cdot\mathbf{x}}\boldsymbol{H}_p(\mathbf{x}), \tag{3}$$

where $\mathbf{k}\in\mathbb{R}^3$ is the wave vector in the first Brillouin zone (FBZ) [12] and $\boldsymbol{E}_p(\mathbf{x})$ and $\boldsymbol{H}_p(\mathbf{x})$ are periodic in conformity with (1), i.e.,

$$\boldsymbol{E}_p(\mathbf{x}+\mathbf{a}_\ell)=\boldsymbol{E}_p(\mathbf{x}), \quad \boldsymbol{H}_p(\mathbf{x}+\mathbf{a}_\ell)=\boldsymbol{H}_p(\mathbf{x}), \quad \ell=1,2,3. \tag{4}$$

Plugging (3) into (2) and noticing the following vector calculus identities

$$\mathrm{e}^{-\imath\mathbf{k}\cdot\mathbf{x}}\nabla\times(\mathrm{e}^{\imath\mathbf{k}\cdot\mathbf{x}}\boldsymbol{E}_p)=(\imath\mathbf{k}+\nabla)\times\boldsymbol{E}_p, \quad \mathrm{e}^{-\imath\mathbf{k}\cdot\mathbf{x}}\nabla\cdot(\mathrm{e}^{\imath\mathbf{k}\cdot\mathbf{x}}\boldsymbol{E}_p)=(\imath\mathbf{k}+\nabla)\cdot\boldsymbol{E}_p,$$

MEQs (2) can be recast into

$$(\imath\mathbf{k}+\nabla)\times\boldsymbol{E}_p=\imath\omega\mu\boldsymbol{H}_p, \quad -(\imath\mathbf{k}+\nabla)\times\boldsymbol{H}_p=\imath\omega\varepsilon\boldsymbol{E}_p, \tag{5a}$$

$$(\imath\mathbf{k}+\nabla)\cdot(\mu\boldsymbol{H}_p)=0, \qquad (\imath\mathbf{k}+\nabla)\cdot(\varepsilon\boldsymbol{E}_p)=0. \tag{5b}$$

In the case of non-dispersive PCs, usually the wave vector $\mathbf{k}\in\mathbb{R}^3$ is chosen beforehand, and MEQs (2) are discretized into a constrained eigenvalue problems w.r.t. ω. By solving a few smallest positive ω's for different $\mathbf{k}$, we obtain the dispersion curves $\omega=\omega(\mathbf{k})$ or the standard band structures (SBSs). Notably, we have recently established a fast algorithm in [6, 7] for this task.

In the case of dispersive PCs, due to the highly nonlinear dependence of ε or μ on ω, it is far more challenging to compute the dispersion curves $\omega = \omega(\mathbf{k})$, as shown in [8]. However, as evidenced by several works [3, 4, 13], for dispersive PCs, it is much more convenient to adopt an opposite perspective that the wave vector $\mathbf{k}$ is viewed as a function $\mathbf{k} = \mathbf{k}(\omega)$ of the real frequency ω. In other words, in this case, it is much easier to compute the complex band structure (CBS) $\mathbf{k} = \mathbf{k}(\omega)$, i.e., to solve $\mathbf{k} \in \mathbb{C}^3$ such that $\omega(\mathbf{k})$ is equal to a positive constant, as well as the associated field quantities which satisfy MEQs (5). Moreover, among applications mentioned in [4], the CBS is fundamentally important for computing the density of states of PCs, which is similar to the case in solid-state physics and mesoscopic electron transport [10]. In practice, to further simplify the computation, we may fix the direction vector $\tilde{\mathbf{k}} = [\tilde{k}_1, \tilde{k}_2, \tilde{k}_3]^\top \in \mathbb{R}^3$ with $\tilde{\mathbf{k}} \cdot \tilde{\mathbf{k}} = 1$ and let $\mathbf{k} = \lambda\tilde{\mathbf{k}}$ in (5) [3, 4, 13]. Then, by assuming $\mu(\mathbf{x}) = \mu_0 = 1$ and eliminating $\boldsymbol{H}_p$, (5) can be reduced into the following constrained quadratic operator pencil (QOP) w.r.t. λ [1],

$$(\imath\lambda\tilde{\mathbf{k}} + \nabla) \times (\imath\lambda\tilde{\mathbf{k}} + \nabla) \times \boldsymbol{E}_p = \omega^2 \varepsilon \boldsymbol{E}_p, \text{ with } (\imath\lambda\tilde{\mathbf{k}} + \nabla) \cdot (\varepsilon \boldsymbol{E}_p) = 0, \ \omega \in \mathbb{R}^+. \quad (6)$$

The aim of this article is to develop an efficient method to solve (6) for the 3D *dispersive* PC and *non-dispersive* PC. For simplicity, hereafter, we only consider *isotropic* ε, i.e., $\varepsilon = \varepsilon(\mathbf{x}, \omega) \colon \mathbb{R}^3 \times \mathbb{R} \to \mathbb{C}$ or $\varepsilon = \varepsilon(\mathbf{x}) \colon \mathbb{R}^3 \to \mathbb{C}$.

Plenty of works have been published during the last three decades on CBS computations, mainly for 2D PCs, using several methods to discretize (6), such as variants of the plane-wave expansion method [5, 13], diagonalizing the transfer matrix [20], and the prevalent finite element method (FEM), etc. In [2, 3, 4], using FEM, the QOP in (6) is discretized into a QEP

$$\left(\tau^2 M + \tau G + K\right) \mathbf{e} = 0, \quad (7)$$

w.r.t. $\tau = \imath\lambda$, whose coefficient matrices are large sparse. As mentioned in [3], if $\varepsilon \in \mathbb{R}$, then the coefficient matrices of (7) are real, and they satisfy

$$M^\top = M, \quad G^\top = -G, \quad K^\top = K, \quad (8)$$

where $M^\top$ denotes the transpose of M. A QEP (7) with the special structure specified in (8) is called a gyroscopic QEP (GQEP). It is known that if τ is an eigenvalue of the GQEP with real coefficients, then so are $-\tau$ and their complex conjugates, $\pm\bar{\tau}$, which is the Hamiltonian structure of the spectrum of a GQEP.

In [2, 4], the GQEP (7) is arbitrarily linearized into a generalized eigenvalue problem (GEP), to which some general purpose sparse eigensolver is applied. It is pointed out in [17] that an arbitray linearization that disrespects the Hamiltonian structure in finite arithmetic will lose pairing of the computed eigenvalues and may cause generally backward stable methods to become unstable. In contrast, the authors of [3] are aware of the Hamiltonian structure of the spectrum of the GQEP (7) for real ε, and literally adopt the structure-preserving approach developed in [17] to solve eigenvalues of the GQEP (7) near or on the imaginary axis but away from the origin. There, the skew-Hamiltonian isotropic implicitly

restarted Arnoldi (SHIRA) algorithm is the workhorse. However, we find that if those eigenvalues the GQEP (7) are desired, it is hard to choose the suitable positive shift needed in the SHIRA algorithm. Besides, the price of extraction of the associated eigenvectors, which are often desired, is high. In addition, it is unclear how to address the problem stemmed from complex ε using the SHIRA algorithm. One main motivation of our present work is to present a superior structure-preserving algorithm that are free from these drawbacks.

Besides, in [1, 6, 7], the merits of using Yee's scheme (YS) [22], which is a special finite difference (FD) scheme, to discretize MEQs (2), especially in 3D cases, have been emphasized. Notably, with YS, the discretized Gauss' and Stokes' laws hold exactly, and the fast Fourier transformation (FFT) can come into play in accelerating SBS computations of 3D non-dispersive PCs. In contrast, if FEM with commonly used basis functions is employed for such tasks, there is hardly any arena for popular fast algorithms. From this perspective, YS is much more attractive. Thus, it is another motivation of this work to develop a fast algorithm with YS for computing CBSs of 3D PCs.

In brief, contributions made in this work are as follows.

- Using YS to discretize (6) yields a large sparse GQEP (7), whose coefficient matrices M and G are always real while K is not real if ε is not real. Consequently, the spectrum of the resulting GQEP always has the Hamiltonian structure no matter whether ε is real or complex. Moreover, the resulting discretized divergence-free condition in (6) holds automatically.

- The GQEP is mapped to a $\top$-parlindromic QEP ($\top$-PQEP) $(\nu^2 A^\top - \nu Q + A)\mathbf{e} = 0$ with $Q^\top = Q$, under the Cayley transformation [10]. Accordingly, the target eigenvalues of the GQEP which are close to the imaginary axis are transformed into eigenvalues of the $\top$-PQEP which are near the unit circle. It is much easier to determine the shift when computing the target eigenvalues of the latter. Via the $\top$-symplectic linearization and the $(\mathcal{S} + \mathcal{S}^{-1})$-transform [14], the $\top$-PQEP is transformed into a $\top$-skew-Hamiltonian pencil, to which a structure-preserving Arnoldi algorithm called G$\top$SHIRA algorithm is applied to practically compute the partial spectrum close to the given shift. Moreover, the associated eigenvectors of (7) can be cheaply computed from those of the $\top$-skew-Hamiltonian pencil that the G$\top$SHIRA algorithm also provides.

- In each iteration of the G$\top$SHIRA algorithm, we need to sequentially solve two linear systems efficiently. To this end, we propose the preconditioning techniques based on explicit eigen-decompositions of three components of discretized $\tilde{\mathbf{k}}\times$ and $\nabla\times$ operators in (6), respectively. More importantly, we show that the preconditioners can be realized using FFT-accelerated matrix-vector multiplications [6, 8, 11]. As manifested by numerical results, the efficiency of our preconditioners turns out to be almost independent of the mesh size of the problem.

This article is outlined as follows. In Sec. 2, discretization of (6) using YS incorporated with (4) is presented. In Sec. 3, our unique way to solve the GQEP

in a fully structure-preserving manner is detailed. In Sec. 4, the preconditioner to speed up the convergence of inner iterations of the G⊤SHIRA algorithm is put forward. In Sec. 5, we present some numerical examples to demonstrate the efficiency and accuracy of our method, including the preconditioner. In Sec. 6 we conclude this work and discuss potential generalizations of our method.

We close this section by introducing some terminologies and notations. $\overline{A}, A^\top$ and A^* denote the complex conjugate, the transpose and the conjugate transpose of A, respectively. I_m denotes the identity matrix of dimension $m \in \mathbb{N}$. $\mathbb{T} := \{z \in \mathbb{C} : \|z\| = 1\}$ refers to the unit circle with $\|\cdot\|$ being the Euclidean norm. $\sigma(A, B)$ denotes the spectrum of the matrix pair (A, B). $\Im$ denotes the imaginary part. $\mathbb{R}^+ := \{x \in \mathbb{R} : x > 0\}$. $A \oplus B$ and $A \otimes B$ denote the direct sum and the Kronecker product of matrices A and B, respectively. Below is the ABC of structured eigenvalue problems. Denote $\mathcal{J}_{2m} := \begin{bmatrix} 0 & I_m \\ -I_m & 0 \end{bmatrix}$.

(i) $\mathcal{H} \in \mathbb{C}^{2m\times 2m}$ is called a $\top$-skew-Hamiltonian matrix if $(\mathcal{H}\mathcal{J}_{2m})^\top = -\mathcal{H}\mathcal{J}_{2m}$. $\mathcal{K} - \lambda\mathcal{N} \in \mathbb{C}^{2m\times 2m}$ is called a $\top$-skew-Hamiltonian pencil if both $\mathcal{K}$ and $\mathcal{N}$ are $\top$-skew-Hamiltonian.

(ii) $\mathcal{U} \in \mathbb{C}^{2m\times 2m}$ is called a $\top$-symplectic matrix if $\mathcal{U}^\top\mathcal{J}_{2m}\mathcal{U} = \mathcal{J}_{2m}$; $\mathcal{M}-\lambda\mathcal{L} \in \mathbb{C}^{2m\times 2m}$ is called a $\top$-symplectic pencil if $\mathcal{M}\mathcal{J}_{2m}\mathcal{M}^\top = \mathcal{L}\mathcal{J}_{2m}\mathcal{L}^\top$.

(iii) $X, Y \in \mathbb{C}^{2m\times l}, 1 \le l \le n$, are called $\top$-bi-isotropic if $X^\top\mathcal{J}_{2m}Y = 0$.

Hereinafter, for convenience, we will drop the subscripts of notations I_m, $\mathcal{J}_{2m}$ and $\boldsymbol{E}_p$ whenever no confusion arises. We will frequently employ the MATLAB programming language in this work without prior notification. The vectorization of an array X of any shape is denoted by $\mathrm{vec}(X)$, i.e., $\mathrm{vec}(X) = X(:)$. δ_i^j is the Kronecker delta function, i.e., $\delta_i^j := (i==j)$.

2. Discretization of (6) with YS

Recently in [7], we have presented the discretization of MEQs (2) using YS and developed some fast algorithms of SBS computations for 3D isotropic non-dispersive PCs with all fourteen Bravais lattices. There, the Bloch condition is imposed on $\mathbf{E}(\mathbf{x})$ and $\mathbf{H}(\mathbf{x})$ in (3), i.e., $\mathbf{E}(\mathbf{x}+\mathbf{a}_\ell) = \exp(\imath\mathbf{k}\cdot\mathbf{a}_\ell)\mathbf{E}(\mathbf{x})$, $\mathbf{H}(\mathbf{x}+\mathbf{a}_\ell) = \exp(\imath\mathbf{k}\cdot\mathbf{a}_\ell)\mathbf{H}(\mathbf{x})$, $\ell = 1, 2, 3$. We notice that by simply setting $\mathbf{k} = 0$ in (3), the discretized $\nabla\times$ operators obtained in [7] can be literally employed as the discretization of $\nabla\times$ operators appearing in (5) and (6). From [7] we know that the contents of the coefficient matrices in (7) are specific to the underlying Bravais lattice, however, it is not the objective of this work to list all possible results. Throughout this work we decide to take the body centered cubic (BCC) lattice for example to illuminate the discretization of (6). For comparison, we also put some formulas for the simple cubic lattice in AppendixA. Other Bravais lattices can be processed likewise.

Lattice translation vectors $\mathbf{a}_1, \mathbf{a}_2$ and $\mathbf{a}_3$ of the BCC lattice [19] (also see Fig. 2(a)) are $[\mathbf{a}_1, \mathbf{a}_2, \mathbf{a}_3] = \frac{\tilde{a}}{2}\begin{bmatrix} -1 & 1 & 1 \\ 1 & -1 & 1 \\ 1 & 1 & -1 \end{bmatrix}$, where $\tilde{a}$ is the lattice constant.

In order to apply YS, usually orthogonal meshes are needed. Following [7], an appropriate set of orthogonal basis $\{\mathbf{a},\mathbf{b},\mathbf{c}\}$ of $\{\mathbf{a}_\ell\}_{\ell=1}^3$ should be determined. Actually, in this case, $\mathbf{a}=\mathbf{a}_1$, $\mathbf{b}=\mathbf{a}_2+\mathbf{a}_1/3$, and $\mathbf{c}=\mathbf{a}_3+\mathbf{a}_1/2+\mathbf{a}_2/2$, with $a:=\|\mathbf{a}\|=\sqrt{3}\tilde{a}/2$, $b:=\|\mathbf{b}\|=\sqrt{6}\tilde{a}/3$ and $c:=\|\mathbf{c}\|=\sqrt{2}\tilde{a}/2$.

Naturally, we identify $\mathbf{a}/a,\mathbf{b}/b,\mathbf{c}/c$ as unit vectors of x-,y-,z-axes of an orthogonal coordinate system, and dub the cuboid cell $\Omega_c=[0,a]\times[0,b]\times[0,c]$ as the computational cell, where YS can be conveniently applied. The computational cell Ω_c is uniformly partitioned into small cuboid cells whose edge lengths along x-, y- and z-directions are $\delta_x=a/n_1$, $\delta_y=b/n_2$ and $\delta_z=c/n_3$, respectively, with $n_1,n_2,n_3\in\mathbb{N}$. For convenience, we introduce the function

$$\mathbf{x}(r,s,t):=(r\delta_x,s\delta_y,t\delta_z),\quad r,s,t\in\mathbb{R},$$

to represent a point $(r\delta_x,s\delta_y,t\delta_z)$ in this orthogonal coordinate system. Since only points $\mathbf{x}(r,s,t)\in\Omega_c$ with $(r,s,t)\in[0,n_1]\times[0,n_2]\times[0,n_3]$ are involved in the simulation, we have to reformulate (4) in terms of $\mathbf{a},\mathbf{b}$ and $\mathbf{c}$.

Specifically, with $r\in[0,n_1)$, $s\in[0,n_2)$, $t\in[0,n_3)$, we have

$$\boldsymbol{E}(\mathbf{x}(n_1,s,t))=\boldsymbol{E}(\mathbf{x}(0,s,t)+\mathbf{a})=\boldsymbol{E}(\mathbf{x}(0,s,t)),\tag{9a}$$

$$\boldsymbol{E}(\mathbf{x}(r,n_2,t))=\boldsymbol{E}(\mathbf{x}(r,0,t)+\mathbf{b})=\boldsymbol{E}(\mathbf{x}(\tilde{r}_2,0,t)),\tag{9b}$$

$$\boldsymbol{E}(\mathbf{x}(r,s,n_3))=\boldsymbol{E}(\mathbf{x}(r,s,0)+\mathbf{c})=\boldsymbol{E}(\mathbf{x}(\tilde{r}_3,\tilde{s}_3,0)),\tag{9c}$$

where in (9b) $\tilde{r}_2=r+2n_1/3$ if $r<n_1/3$, while $\tilde{r}_2=r-n_1/3$ if $r\geq n_1/3$; in (9c) $\tilde{r}_3=r+n_1/2$ if $r<n_1/2$, while $\tilde{r}_2=r-n_1/2$ if $r\geq n_1/2$; in (9c) $\tilde{s}_3=s+n_2/2$ if $s<n_2/2$, while $\tilde{s}_3=s-n_2/2$ if $s\geq n_2/2$. In passing, we can always make $n_1/3$, $n_1/2$ and $n_2/2$ integers. (9a)–(9c) constitute the periodic boundary condition of our problem in Ω_c, which $\boldsymbol{H}(\mathbf{x})$ also satisfies.

In YS, the components $\boldsymbol{E}$ are sampled at midpoints of all edges, and the components of $\boldsymbol{H}$ are sampled at all face centers. To conveniently index all these sampling points, we introduce three index sets

$$\mathbb{N}_\ell:=\{0,1,\ldots,n_\ell-1\},\quad \ell=1,2,3,\tag{10}$$

and the shorthand notations $\hat{i}:=i+1/2$, $\hat{j}:=j+1/2$, $\hat{k}:=k+1/2$. For example, $\{\mathbf{x}(\hat{i},j,k):i\in\mathbb{N}_1,j\in\mathbb{N}_2,k\in\mathbb{N}_3\}$—the set of coordinates of midpoints of all edges along x-direction, is naturally viewed as a three-way array stored in the column-major order, i.e., the index i varies fastest and k varies slowest. So is the set of corresponding samples of electric field $\{E_1(\mathbf{x}(\hat{i},j,k)):i\in\mathbb{N}_1,j\in\mathbb{N}_2,k\in\mathbb{N}_3\}$. The set of samples of E_2,E_3,H_1,H_2 and H_3 are similarly treated. Then, we can compactly define the following six column vectors of length $n:=n_1n_2n_3$,

$$\mathbf{e}_l=\mathrm{vec}(E_l(\mathbf{x}(0{:}n_1-1,0{:}n_2-1,0{:}n_3-1)+(\delta_l^1,\delta_l^2,\delta_l^3)/2)),\ l=1,2,3,\tag{11}$$

$$\mathbf{h}_l=\mathrm{vec}(H_l(\mathbf{x}(\hat{0}{:}\hat{n}_1-1,\hat{0}{:}\hat{n}_2-1,\hat{0}{:}\hat{n}_3-1)-(\delta_l^1,\delta_l^2,\delta_l^3)/2)),\ l=1,2,3,\tag{12}$$

using the Kronecker delta $\delta_{l'}^l$.

Besides the curl operator $\nabla\times$, whose discretization has been detailed in [7], here in (5) and (6) we have to consider the discretization of the cross-product

operator $\tilde{\mathbf{k}}\times$ as well. The resemblance between $\nabla \times \boldsymbol{E}$ and $\tilde{\mathbf{k}} \times \boldsymbol{E}$ suggests that the components of $\tilde{\mathbf{k}} \times \boldsymbol{E}$ at all face centers be approximated by the linear interpolation between two points. For example, corresponding to

$$\partial_x E_2\Big|_{\mathbf{x}(\hat{i},\hat{j},k)} \approx \frac{E_2(\mathbf{x}(i+1,\hat{j},k)) - E_2(\mathbf{x}(i,\hat{j},k))}{\delta_x}, \tag{13a}$$

we have the approximation

$$\tilde{k}_1 E_2\Big|_{\mathbf{x}(\hat{i},\hat{j},k)} \approx \tilde{k}_1 \frac{E_2(\mathbf{x}(i+1,\hat{j},k)) + E_2(\mathbf{x}(i,\hat{j},k))}{2}. \tag{13b}$$

Therefore, to discretize the cross-product operator $\tilde{\mathbf{k}}\times$, we change the subtraction in the FD formula to the summation and then replace the factor $1/\delta_x, 1/\delta_y$ and $1/\delta_z$ by $\tilde{\mathbf{k}}_1/2, \tilde{\mathbf{k}}_2/2$ and $\tilde{\mathbf{k}}_3/2$, respectively.

The periodic boundary condition (9) do cause complications in determining the correct indices in $\mathbf{e}_l$ and $\mathbf{h}_l, l = 1,2,3$, when partial derivatives of $\boldsymbol{E}$ and $\boldsymbol{H}$ are sampled near Ω_c's boundary surfaces. These difficulties have been systematically resolved in [6, 7]. So here we tersely present the discretization of (5a) with $\mathbf{k} = \lambda\tilde{\mathbf{k}}$, using (12) and (11), as follows:

$$-\imath\omega D_{\varepsilon,l}\mathbf{e}_l = \sum_{p,q=1}^{3} \epsilon_{lpq}(-C_p^\top)\mathbf{h}_q + \imath\lambda \sum_{p,q=1}^{3} \epsilon_{lpq}\widetilde{C}_p^\top \mathbf{h}_q,\ l = 1,2,3, \tag{14a}$$

$$\imath\omega\mathbf{h}_l = \sum_{p,q=1}^{3} \epsilon_{lpq} C_p \mathbf{e}_q + \imath\lambda \sum_{p,q=1}^{3} \epsilon_{lpq}\widetilde{C}_p \mathbf{e}_q,\ l = 1,2,3, \tag{14b}$$

where ϵ_{lpq} is the Levi-Civita symbol in 3D, and

$$D_{\varepsilon,l} = \mathbf{diag}(\mathrm{vec}(\varepsilon(\mathbf{x}(0\!:\!n_1-1, 0\!:\!n_2-1, 0\!:\!n_3-1) + (\delta_l^1, \delta_l^2, \delta_l^3)/2))),\ l = 1,2,3,$$

$$C_1 = I_{n_3} \otimes I_{n_2} \otimes (K_1 - I_{n_1})/\delta_x,\ \widetilde{C}_1 = \widetilde{k}_1 I_{n_3} \otimes I_{n_2} \otimes (K_1 + I_{n_1})/2, \tag{15a}$$

$$C_2 = I_{n_3} \otimes (K_2 - I_{n_1 n_2})/\delta_y, \qquad \widetilde{C}_2 = \widetilde{k}_2 I_{n_3} \otimes (K_2 + I_{n_1 n_2})/2, \tag{15b}$$

$$C_3 = (K_3 - I_n)/\delta_z, \qquad \widetilde{C}_3 = \widetilde{k}_3 (K_3 + I_n)/2, \tag{15c}$$

with

$$K_1 = \begin{bmatrix} 0 & I_{n_1-1} \\ 1 & 0 \end{bmatrix},\ K_2 = \begin{bmatrix} 0 & I_{n_1(n_2-1)} \\ J_2 & 0 \end{bmatrix},\ K_3 = \begin{bmatrix} 0 & I_{n_1 n_2(n_3-1)} \\ J_3 & 0 \end{bmatrix}, \tag{15d}$$

$$J_2 = \begin{bmatrix} 0 & I_{2n_1/3} \\ I_{n_1/3} & 0 \end{bmatrix},\ J_3 = \begin{bmatrix} 0 & & I_{n_2/2} \otimes \begin{bmatrix} 0 & I_{2n_1/3} \\ I_{n_1/3} & 0 \end{bmatrix} \\ I_{n_2/2} \otimes \begin{bmatrix} 0 & I_{n_1/3} \\ I_{2n_1/3} & 0 \end{bmatrix} & & 0 \end{bmatrix}.$$

Further, we define

$$\mathbf{e} := [\mathbf{e}_1^\top\ \mathbf{e}_2^\top\ \mathbf{e}_3^\top]^\top,\ \mathbf{h} := [\mathbf{h}_1^\top\ \mathbf{h}_2^\top\ \mathbf{h}_3^\top]^\top \in \mathbb{C}^{3n},\ D_\varepsilon := D_{\varepsilon,1} \oplus D_{\varepsilon,2} \oplus D_{\varepsilon,3},$$

$$C := \begin{bmatrix} 0 & -C_3 & C_2 \\ C_3 & 0 & -C_1 \\ -C_2 & C_1 & 0 \end{bmatrix}, \quad \text{and} \quad \widetilde{C} := \begin{bmatrix} 0 & -\widetilde{C}_3 & \widetilde{C}_2 \\ \widetilde{C}_3 & 0 & -\widetilde{C}_1 \\ -\widetilde{C}_2 & \widetilde{C}_1 & 0 \end{bmatrix}, \tag{16}$$

then we can recast (14) into

$$(-\imath\lambda\widetilde{C} + C)^\top \mathbf{h} = -\imath\omega D_\varepsilon \mathbf{e}, \quad (\imath\lambda\widetilde{C} + C)\mathbf{e} = \imath\omega\mathbf{h}. \tag{17}$$

Elimination of $\mathbf{h}$ in (17) yields the discretization of the QOP in (6) as follows,

$$(-\imath\lambda\widetilde{C} + C)^\top (\imath\lambda\widetilde{C} + C)\mathbf{e} = \omega^2 D_\varepsilon \mathbf{e}, \tag{18}$$

which is a QEP w.r.t. λ, for a given $\omega \in \mathbb{R}^+$. Moreover, following (13) and (14), we can easily discretize the divergence-free constraint in (6) into

$$\left(\imath\lambda \begin{bmatrix} \widetilde{C}_1^\top & \widetilde{C}_2^\top & \widetilde{C}_3^\top \end{bmatrix} - \begin{bmatrix} C_1^\top & C_2^\top & C_3^\top \end{bmatrix}\right) D_\varepsilon \mathbf{e} = 0. \tag{19}$$

Thus, (6) is discretized into a QEP (18) with the constraint (19). Here, analogous to the SBS calculations of 3D non-dispersive PCs with YS [6, 7], we can show that (19) holds automatically if the same $\mathbf{e}$ satisfies (18) with $\omega > 0$, so that we are merely concerned about (18).

First of all we would like to point out some basic facts.

Lemma 1. *$\{C_\ell, C_\ell^\top, \widetilde{C}_\ell, \widetilde{C}_\ell^\top\}_{\ell=1}^3$ in (15) is a set of commutative matrices, and C commutes with $\widetilde{C}$ in (16).*

The elegant proof of Lemma 1 can be found in [7], which draws on some nice properties of unitary (block) companion matrices. Denote

$$P_0(\tau) = \tau \begin{bmatrix} \widetilde{C}_1^\top & \widetilde{C}_2^\top & \widetilde{C}_3^\top \end{bmatrix} + \begin{bmatrix} C_1^\top & C_2^\top & C_3^\top \end{bmatrix}, \quad \tau \in \mathbb{C}, \tag{20}$$

then from Lemma 1 one can easily verify the following identity,

$$P_0(\tau)(\tau\widetilde{C} + C)^\top = 0. \tag{21}$$

Multiplying both sides of (18) by $P_0(-\imath\lambda)$ and using (21), we immediately have

Theorem 1. *The discretized divergence-free constraint in (19) holds automatically for an eigenvector $\mathbf{e}$ of (18) with $\omega \in \mathbb{R}^+$.*

3. The structure-preserving algorithm for large $\top$-PQEP

In fact, we let $\tau = \imath\lambda$ and define

$$K := \omega^2 D_\varepsilon - C^\top C = K^\top \in \mathbb{C}^{3n\times 3n}, \tag{22a}$$

$$G := \widetilde{C}^\top C - C^\top \widetilde{C} = -G^\top \in \mathbb{R}^{3n\times 3n}, \tag{22b}$$

$$M := \widetilde{C}^\top \widetilde{C} = M^\top \in \mathbb{R}^{3n\times 3n}, \tag{22c}$$

then the QEP (18) proves a GQEP w.r.t. τ as follows,

$$\mathcal{Q}_g(\tau)\mathbf{e} := (\tau^2 M + \tau G + K)\mathbf{e} = \mathbf{0}. \tag{23}$$

It is worth recognizing the Hamiltonian structure of the spectrum of a GQEP.

Proposition 1. *The eigenvalues of a GQEP form doublet $\{\tau, -\tau\}$, and they form quadruplet $\{\tau, \overline{\tau}, -\tau, -\overline{\tau}\}$ if the coefficient matrices are real and $\tau \notin \mathbb{R} \cup \imath\mathbb{R}$.*

Remark 1. *Even if the permittivity ε is not a real function, and more generally, even if K, M and G in (22) are all complex matrices, the Hamiltonian structure of the spectrum of the GQEP (23) persists.*

3.1. Cayley transformation and the $\top$-PQEP

Assuming $\tau \neq \pm 1$, we can introduce the Cayley transformation

$$\nu = \pm\frac{1+\tau}{1-\tau}, \quad \text{i.e.,} \quad \tau = \frac{\nu \mp 1}{\nu \pm 1}, \tag{24}$$

to achieve the bijection between a GQEP (23) and a $\top$-PQEP. Specifically, substitution of (24) into (23) yields a $\top$-PQEP w.r.t. ν,

$$\mathcal{Q}_p(\nu)\mathbf{e} := \frac{1}{4}(\nu \pm 1)^2 \mathcal{Q}_g\left(\frac{\nu \mp 1}{\nu \pm 1}\right)\mathbf{e} := (\nu^2 A^\top - \nu Q + A)\mathbf{e} = \mathbf{0}, \tag{25a}$$

where

$$A = (M - G + K)/4 \in \mathbb{C}^{3n\times 3n}, \quad Q = \pm(M-K)/2 = Q^\top \in \mathbb{C}^{3n\times 3n}. \tag{25b}$$

Similar to Proposition 1, one should recognize the symplectic structure of the spectrum of a $\top$-PQEP (25a).

Proposition 2. *The eigenvalues of a $\top$-PQEP form doublet $\{\nu, \nu^{-1}\}$ and they form quadruplet $\{\nu, \overline{\nu}, \nu^{-1}, \overline{\nu}^{-1}\}$ if the coefficient matrices are real and $\nu \notin \mathbb{T}$.*

By introducing $\breve{\mathbf{e}} = A\mathbf{e}/\nu$, we linearize the $\top$-PQEP (25a) into,

$$\mathcal{M}\begin{bmatrix}\mathbf{e}\\ \breve{\mathbf{e}}\end{bmatrix} = \nu\mathcal{L}\begin{bmatrix}\mathbf{e}\\ \breve{\mathbf{e}}\end{bmatrix}, \tag{26}$$

where

$$\mathcal{M} = \begin{bmatrix}A & 0\\ Q & -I\end{bmatrix}, \quad \mathcal{L} = \begin{bmatrix}0 & I\\ A^\top & 0\end{bmatrix}. \tag{27}$$

It is easy to see that the matrix pair $(\mathcal{M}, \mathcal{L})$ in (27) satisfies $\mathcal{M}\mathcal{J}\mathcal{M}^\top = \mathcal{L}\mathcal{J}\mathcal{L}^\top$, i.e., it is a $\top$-symplectic pair [9]. Thus, the twin eigenvalues $(\nu, 1/\nu)$ of $(\mathcal{M}, \mathcal{L})$ always come together, including $(0, \infty) := (0, 1/0)$, which exactly inherits the symplectic property mentioned in Proposition 2.

The $(\mathcal{S}+\mathcal{S}^{-1})$-transform $(\mathcal{M}_s, \mathcal{L}_s)$ of the matrix pair $(\mathcal{M}, \mathcal{L})$ defined as [14]

$$\mathcal{M}_s := \mathcal{M}\mathcal{J}\mathcal{L}^\top + \mathcal{L}\mathcal{J}\mathcal{M}^\top, \quad \mathcal{L}_s := \mathcal{L}\mathcal{J}\mathcal{L}^\top,$$

is further equivalent to a $\top$-skew-Hamiltonian pair $(\mathcal{K},\mathcal{N})$ with

$$\mathcal{K} := \mathcal{M}_s\mathcal{J}^\top = \begin{bmatrix} Q & A-A^\top \\ A^\top - A & Q \end{bmatrix}, \quad \mathcal{N} := \mathcal{L}_s\mathcal{J}^\top = \begin{bmatrix} A & 0 \\ 0 & A^\top \end{bmatrix}. \tag{28}$$

In other words, solving the GEP (26) is now reduced to solving the GEP

$$\mathcal{K}\mathbf{u} = \eta\mathcal{N}\mathbf{u} \tag{29}$$

of a $\top$-skew-Hamiltonian pair $\mathcal{K}$ and $\mathcal{N}$. The relation between eigenpairs of $(\mathcal{M},\mathcal{L})$ and those of $(\mathcal{K},\mathcal{N})$ is unveiled in Theorem 2, also in [9].

Theorem 2. *Let $(\mathcal{M},\mathcal{L})$ defined in (27) and $(\mathcal{K},\mathcal{N})$ in (28), then*

(i) *η is a double eigenvalue of $(\mathcal{K},\mathcal{N})$ if and only if $\nu, 1/\nu$ are eigenvalues of $(\mathcal{M},\mathcal{L})$, where $\nu, 1/\nu$ are two roots of the equation $\eta = \nu + 1/\nu$.*

(ii) *If $(\eta, [\mathbf{u}_1^\top \ \mathbf{u}_2^\top])^\top$ is an eigenpair of $(\mathcal{K},\mathcal{N})$ with $\eta = \nu + \nu^{-1} \neq 2$, then*

$$\begin{bmatrix} \mathbf{v}_1 \\ \breve{\mathbf{v}}_1 \end{bmatrix} = \begin{bmatrix} \nu^{-1}\mathbf{u}_1 - \mathbf{u}_2 \\ Q\mathbf{v}_1 - \nu A^\top \mathbf{v}_1 \end{bmatrix}, \quad \begin{bmatrix} \mathbf{v}_2 \\ \breve{\mathbf{v}}_2 \end{bmatrix} = \begin{bmatrix} \nu\mathbf{u}_1 - \mathbf{u}_2 \\ Q\mathbf{v}_2 - \nu^{-1} A^\top \mathbf{v}_2 \end{bmatrix}$$

are the eigenvectors of $(\mathcal{M},\mathcal{L})$ corresponding to ν and $1/\nu$, respectively.

Before discussing the eigensolver for the large sparse $\top$-skew-Hamiltonian pencil, we would like to summarize several relevant eigenvalue problems we have encountered in this section as follows,

(i) the QEP (18) w.r.t. λ;
(ii) the GQEP (23) w.r.t. $\tau = \imath\lambda$;
(iii) the $\top$-PQEP (25a) and $\top$-symplectic GEP (26) w.r.t. $\nu = \pm(1+\tau)/(1-\tau)$;
(iv) the $\top$-skew-Hamiltonian GEP (29) w.r.t. $\eta = \nu + 1/\nu$.

They are briefly put in the following chains

$$\lambda \in \mathbb{R} \Longleftrightarrow \tau \in \imath\mathbb{R} \Longleftrightarrow \nu \in \mathbb{T} \Longleftrightarrow \eta \in [-2,2],$$
$$|\Im\lambda| \ll 1, \lambda \notin \mathbb{R} \Longleftrightarrow 0 < \big||\nu| - 1\big| \ll 1 \Longleftrightarrow 0 < \operatorname{dist}(\eta, [-2,2]) \ll 1,$$

where $\operatorname{dist}(\eta,[-2,2])$ denotes the distance between $\eta \in \mathbb{C}$ and the segment $[-2,2] \subset \mathbb{R}$. To give the reader a perception of how the distribution of the spectrum changes under the above mentioned spectral transformations, we just take the QEP (18) with matrix dimension $3n = 192$ for example. In Fig. 1, we plot some λ's, i.e., eigenvalues of this QEP, with small magnitude, and their images under the mapping $\nu = -(1+\imath\lambda)/(1-\imath\lambda)$ and $\eta = -2(1-\lambda^2)/(1+\lambda^2)$, respectively. We can clearly see that in Fig. 1(c) the target eigenvalues are well separated from the unwanted eigenvalues, compared with those in Fig. 1(a). Moreover, in Fig. 1(b) the unwanted eigenvalues are clustered around -1, therefore it is better to choose the suitable shift to the right of $\pm 1\imath$ in order to stay away from the singularity. When a shift is given, the G$\top$SHIRA algorithm will likely converge much faster than other eigensolvers that directly deal with λ.

In a word, the desired eigenvalues of the original problem (18) are transformed into the eigenvalues of the resulting $\top$-skew-Hamiltonian pencil $(\mathcal{K},\mathcal{N})$ in (28) which are located near or in $[-2,2]$. As a consequence, in effect we can concentrate on the interval $[-2,2]$ to choose the suitable shifts that are needed in the G$\top$SHIRA algorithm discussed below to compute eigenvalues of $(\mathcal{K},\mathcal{N})$.

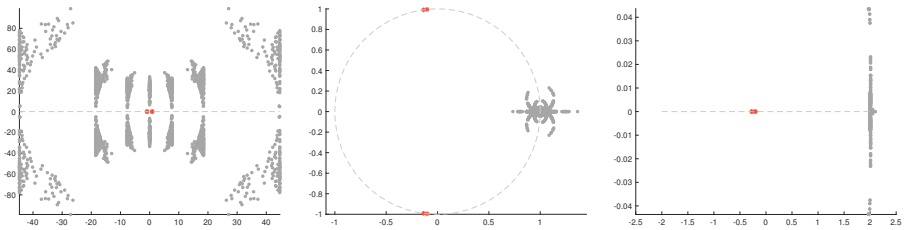

(a) The distribution of λ's with $|\lambda| < 100$. (b) The image of those λ's under $\nu = \nu(\lambda)$. (c) The image of those λ's under $\eta = \eta(\lambda)$.

Figure 1: The partial distribution of (a) λ and (b) $\nu = \nu(\lambda) = -(1+\imath\lambda)/(1-\imath\lambda)$ and (c) $\eta = \eta(\lambda) = -2(1-\lambda^2)/(1+\lambda^2)$. The desired eigenvalues are marked in red, while the unwanted are in grey.

3.2. G⊤SHIRA algorithm for $(\mathcal{K},\mathcal{N})$

Suppose some eigenvalues of the $\top$-symplectic pair $(\mathcal{M},\mathcal{L})$ near ν_0 are wanted, with $\nu_0 \notin \sigma(\mathcal{M},\mathcal{L})$. Letting $\eta_0 = \nu_0 + 1/\nu_0 \notin \sigma(\mathcal{K},\mathcal{N})$, the shift-and-invert transformation $(\widehat{\mathcal{K}} - \widehat{\eta}\widehat{\mathcal{N}})$ of $(\mathcal{K}-\eta\mathcal{N})$ with shift $\eta_0 \in \mathbb{C}$ is defined as

$$\widehat{\mathcal{K}} \equiv -\nu_0\mathcal{N} = -\nu_0\mathcal{L}\mathcal{J}_{2n}\mathcal{L}^\top\mathcal{J}_{2n}^\top, \tag{30a}$$

$$\widehat{\mathcal{N}} \equiv -\nu_0\left(\mathcal{K}-\eta_0\mathcal{N}\right) = \left(\mathcal{M}-\nu_0\mathcal{L}\right)\mathcal{J}_{2n}\left(\mathcal{M}^\top-\nu_0\mathcal{L}^\top\right)\mathcal{J}_{2n}^\top, \tag{30b}$$

where both $\widehat{\mathcal{K}}$ and $\widehat{\mathcal{N}}$ are still $\top$-skew-Hamiltonian and $\hat{\eta} = 1/(\eta-\eta_0)$. The G⊤SHIRA, which is short for the generalized $\top$-skew-Hamiltonian implicitly restarted shift-and-invert Arnoldi, algorithm has been developed in [9] to compute the outermost spectrum of $(\widehat{\mathcal{K}},\widehat{\mathcal{N}})$. The G⊤SHIRA algorithm in Algorithm 1 generates a generalized Arnoldi factorization of order m:

$$\widehat{\mathcal{K}}Z_m = Y_mH_m + \mathbf{h}_m(m+1)\mathbf{y}_{m+1}I_m(m,:),$$
$$\widehat{\mathcal{N}}Z_m = Y_mR(1\!:\!m,1\!:\!m),$$

where Y_m and Z_m are $\top$-bi-isotropic and H_m is an upper Hessenberg matrix which stores $\mathbf{h}_1,\cdots,\mathbf{h}_m$, and $R(1\!:\!m,1\!:\!m)$ is an upper triangular matrix.

Note that the step 1 in Algorithm 1, i.e., to solve the linear system $\widehat{\mathcal{N}}\mathbf{z}_j = \mathbf{y}_j$, is the main difficulty of this algorithm. Substituting the following decomposition

$$\mathcal{M}-\nu_0\mathcal{L} = \begin{bmatrix} I & \nu_0 I \\ 0 & I \end{bmatrix}\begin{bmatrix} \mathcal{Q}_p(\nu_0) & 0 \\ 0 & -I \end{bmatrix}\begin{bmatrix} I & 0 \\ -Q+\nu_0A^\top & I \end{bmatrix}$$

into (30b), we see that the task of solving the linear system $\widehat{\mathcal{N}}\mathbf{z}_j = \mathbf{y}_j$ is in effect reduced into sequentially solving two linear systems of halved dimension,

$$\mathcal{Q}_p(\nu_0)\mathbf{u}_1 = \mathbf{b}_1 \quad \text{and} \quad \mathcal{Q}_p(\nu_0)^\top\mathbf{u}_2 = \mathbf{b}_2. \tag{31}$$

We conclude this section with Algorithm 2 to compute eigenpairs of the GQEP (23) via the equivalent $\top$-PQEP (25a). In passing, we also call ν_0 in (31) as shift, since it gives the shift η_0 directly needed in the G⊤SHIRA algorithm.

Algorithm 1 [9] The m-th generalized $\top$-isotropic Arnoldi step

Input: $\top$-skew-Hamiltonian $\widehat{\mathcal{K}}$ and $\widehat{\mathcal{N}}$, upper triangular $R(1\!:\!m-1,1\!:\!m-1)$, orthonormal frames $Z_{m-1}(:,1\!:\!m-1)$ and $Y_m(:,1\!:\!m)$ with $Y_m^\top \mathcal{J} Z_{m-1}=0$.
Output: $\mathbf{h}_m(1\!:\!m+1), R(1\!:\!m,m), \mathbf{y}_{m+1}$ and $\mathbf{z}_m$.

1: Solve $\widehat{\mathcal{N}}\mathbf{z}_m=\mathbf{y}_m$;
2: Compute $\mathbf{r}_m:=Z_{m-1}^*\mathbf{z}_m,\ \ \mathbf{z}_m=\mathbf{z}_m-Z_{m-1}\mathbf{r}_m$;
3: Reorthogonalize $\mathbf{z}_m$ to $\mathcal{J}\overline{Y}_m$ as Step 4 does:
4: $\mathbf{z}_m=\mathbf{z}_m-\mathcal{J}\overline{Y}_m Y_m^\top \mathcal{J}^\top \mathbf{z}_m$;
5: Set $R(m,m):=\|\mathbf{z}_m\|^{-1}$, $\mathbf{z}_m:=R(m,m)\mathbf{z}_m$ and $R(1\!:\!m-1,m):=-R(m,m)R(1\!:\!m-1,1\!:\!m-1)\mathbf{r}_m$;
6: Compute $\mathbf{y}_{m+1}=\mathcal{K}\mathbf{z}_m$;
7: Compute $\mathbf{h}_m(1\!:\!m)=Y_m^*\mathbf{y}_{m+1},\ \ \mathbf{y}_{m+1}=\mathbf{y}_{m+1}-Y_m\mathbf{h}_m(1\!:\!m)$;
8: Reorthogonalize $\mathbf{y}_{m+1}$ to $\mathcal{J}[\overline{Z}_{m-1},\overline{\mathbf{z}}_m]$ as Step 9 does:
9: $\mathbf{y}_{m+1}=\mathbf{y}_{m+1}-\mathcal{J}[\overline{Z}_{m-1},\overline{\mathbf{z}}_m][Z_{m-1},\mathbf{z}_m]^\top \mathcal{J}^\top \mathbf{y}_{m+1}$;
10: Set $\mathbf{h}_m(m+1):=\|\mathbf{y}_{m+1}\|$ and $\mathbf{y}_{m+1}:=\mathbf{y}_{m+1}/\mathbf{h}_m(m+1)$.

Algorithm 2 Computing eigenpairs of a GQEP via symplectic linearization

Input: Given matrices A, Q in (25a), a shift ν_0 and the number of desired eigenpairs $n_w\in\mathbb{N}$.
Output: n_w desired eigenpairs with eigenvalues closest to $\eta_0=\nu_0+\nu_0^{-1}$.

1: Compute eigenpairs $\{(\hat{\eta}_m,[\mathbf{u}_{1,m}^\top\ \mathbf{u}_{2,m}^\top]^\top)\}_{m=1}^{n_w}$ of the $\top$-skew-Hamiltonian pair $(\widehat{\mathcal{K}},\widehat{\mathcal{N}})$ using the G$\top$SHIRA algorithm and set $\eta_m=\hat{\eta}_m^{-1}+\eta_0$.
2: For $m=1,\ldots,n_w$, determine ν_m,ν_m^{-1} by solving $\nu^2-(\eta_m+\eta_m^{-1})\nu+1=0$, and form the twin eigenpairs of the $\top$-PQEP (25a), i.e., $(\nu_m,\ \nu_m^{-1}\mathbf{u}_{1,m}-\mathbf{u}_{2,m})$ and $(\nu_m^{-1},\ \nu_m\mathbf{u}_{1,m}-\mathbf{u}_{2,m})$.
3: For $m=1,\ldots,n_w$, compute $\tau_m=(\nu_m\mp 1)\,/\,(\nu_m\pm 1)$ the twin eigenpairs of the GQEP (23), i.e., $(\tau_m,\ \nu_m^{-1}\mathbf{u}_{1,m}-\mathbf{u}_{2,m})$ and $(-\tau_m,\ \nu_m\mathbf{u}_{1,m}-\mathbf{u}_{2,m})$.

4. Preconditioners for (31)

In most cases, the size of the coefficient matrices in $\mathcal{Q}_p(\nu_0)$ is so large that only the iterative linear solver [18] is affordable for (31) and generally some preconditioning is indispensable. The following facts, which derive from Lemma 1, will give us some inspiration for the preconditioning.

Theorem 3. *With $C,\widetilde{C}$ in (16) and $P_0(\tau)$ in (20), we have*

$$(-\tau\widetilde{C}+C)^\top(\tau\widetilde{C}+C)=I_3\otimes(P_0(-\tau)P_0(\tau)^\top)-P_0(\tau)^\top P_0(-\tau), \tag{32a}$$

$$C^\top C=I_3\otimes(P_0(0)P_0(0)^\top)-P_0(0)^\top P_0(0). \tag{32b}$$

Based on (32b), an FFT-based preconditioner has been proposed in [8, 11] for $\mathcal{Q}_g(0)=K$ with the Bloch condition imposed. Now, with the striking analogy between (32b) and (32a), it is expected that a similar preconditioner exists for $\mathcal{Q}_p(\nu_0),\nu_0\in\mathbb{C}$. To show how the FFT finds application here, we need eigen-decompositions of $\widetilde{C}_\ell, C_\ell, \ell=1,2,3$, in (15) as the foundation.

4.1. Eigen-decompositions of $\widetilde{C}_\ell, C_\ell, \ell = 1,2,3$

Properties of the Kronecker product allows us to reduce eigen-decompositions of $\widetilde{C}_\ell, C_\ell, \ell = 1,2,3$ in (15) to those of K_1, K_2 and K_3 in (15d). As mentioned previously, by setting $\mathbf{k} = 0$, the relevant results in [7] can be easily translated into eigen-decompositions of K_1, K_2 and K_3. So we will just present the key results below without proof. Denote $\zeta(\theta) := \exp(\imath 2\pi\theta)$.

Theorem 4. *Let the index sets $\mathbb{N}_1, \mathbb{N}_2$ and $\mathbb{N}_3$ defined in (10). The circulant matrix K_1 in (15d) satisfies, for $i \in \mathbb{N}_1$,*

$$K_1\mathbf{x}_i = \zeta\left(\frac{i}{n_1}\right)\mathbf{x}_i, \quad \mathbf{x}_i = \left[1, \zeta\left(\frac{i}{n_1}\right), \cdots, \zeta\left(\frac{(n_1-1)i}{n_1}\right)\right]^\top. \tag{33}$$

The matrix K_2 in (15d) satisfies

$$K_2(\mathbf{y}_{ji} \otimes \mathbf{x}_i) = \zeta((j + i/3)/n_2)(\mathbf{y}_{ji} \otimes \mathbf{x}_i), \quad i \in \mathbb{N}_1, \quad j \in \mathbb{N}_2,$$

where

$$\mathbf{y}_{ji} = \left[1, \zeta\left(\frac{j+i/3}{n_2}\right), \cdots, \zeta\left(\frac{(n_2-1)(j+i/3)}{n_2}\right)\right]^\top. \tag{34}$$

The matrix K_3 in (15d) satisfies

$$K_3(\mathbf{z}_{kji} \otimes \mathbf{y}_{ji} \otimes \mathbf{x}_i) = \zeta((k + i/2 + j/2)/n_3)(\mathbf{z}_{kji} \otimes \mathbf{y}_{ji} \otimes \mathbf{x}_i),$$

where, for $i \in \mathbb{N}_1,\ j \in \mathbb{N}_2,\ k \in \mathbb{N}_3$,

$$\mathbf{z}_{kji} = \left[1, \zeta\left(\frac{k+i/2+j/2}{n_3}\right), \cdots, \zeta\left(\frac{(n_3-1)(k+i/2+j/2)}{n_3}\right)\right]^\top. \tag{35}$$

Theorem 5. *Eigen-decompositions of C_ℓ and $\widetilde{C}_\ell$ are*

$$C_\ell = T\Lambda_\ell T^*, \quad \widetilde{C}_\ell = T\widetilde{\Lambda}_\ell T^*, \quad \ell = 1,2,3, \tag{36}$$

respectively, where $TT^* = I_n$ and

$$\Lambda_1 = (\Lambda_{n_1} \otimes I_{n_2} \otimes I_{n_3} - I_n)/\delta_x, \quad \widetilde{\Lambda}_1 = \widetilde{k}_1(\Lambda_{n_1} \otimes I_{n_2} \otimes I_{n_3} + I_n)/2, \tag{37a}$$

$$\Lambda_2 = (\oplus_{i=1}^{n_1}\Lambda_{in_2} \otimes I_{n_3} - I_n)/\delta_y, \quad \widetilde{\Lambda}_2 = \widetilde{k}_2(\oplus_{i=1}^{n_1}\Lambda_{in_2} \otimes I_{n_3} + I_n)/2, \tag{37b}$$

$$\Lambda_3 = \left(\oplus_{i=1}^{n_1}\oplus_{j=1}^{n_2}\Lambda_{ijn_3} - I_n\right)/\delta_z, \ \widetilde{\Lambda}_3 = \widetilde{k}_3\left(\oplus_{i=1}^{n_1}\oplus_{j=1}^{n_2}\Lambda_{ijn_3} + I_n\right)/2, \tag{37c}$$

with

$$\Lambda_{n_1} = \mathbf{diag}\left(\zeta([0\!:\!n_1-1]^\top/n_1)\right), \ \Lambda_{in_2} = \mathbf{diag}\left(\zeta(([0\!:\!n_2-1]^\top + i/3)/n_2)\right),$$
$$\Lambda_{ijn_3} = \mathbf{diag}\left(\zeta(([0\!:\!n_3-1]^\top + i/2 + j/2)/n_3)\right),$$

and for $i \in \mathbb{N}_1,\ j \in \mathbb{N}_2,\ k \in \mathbb{N}_3$, with $\mathbf{x}_i, \mathbf{y}_{ji}, \mathbf{z}_{kji}$ in (33), (34), (35), respectively,

$$T(1\!:\!n,\ 1 + k + jn_3 + in_2n_3) = (\mathbf{z}_{kji} \otimes \mathbf{y}_{ji} \otimes \mathbf{x}_i)/\sqrt{n}. \tag{38}$$

4.2. Preconditioner for $\mathcal{Q}_p(\nu_0)$ and $\mathcal{Q}_p(\nu_0)^\top$

Following [8, 11], to make full use of the eigen-decompositions in Theorem 5, we deliberately replace D_ε in (22a) by αI with $\alpha := \mathbf{mean}(\mathbf{diag}(D_\varepsilon))$, and define the following quadratic matrix polynomial

$$\mathcal{P}_g(\tau) = \omega^2\alpha I - (-\tau\widetilde{C} + C)^\top(\tau\widetilde{C} + C) = \mathcal{Q}_g(\tau) + \omega^2(\alpha I - D_\varepsilon), \tag{39}$$

which resembles $\mathcal{Q}_g(\tau)$ very much. Similar to (25a), here we let

$$\mathcal{P}_p(\nu_0) = \frac{1}{4}(\nu_0 \pm 1)^2\mathcal{P}_g(\tau_0) \quad \text{with} \quad \tau_0 = \frac{\nu_0 \mp 1}{\nu_0 \pm 1}, \tag{40}$$

and regard $\mathcal{P}_p(\nu_0)^{-1}$ and $\mathcal{P}_p(\nu_0)^{-\top}$ as the preconditioner for the two linear systems in (31), respectively. Since $\mathcal{Q}_p(\nu_0)^\top = \nu_0^2\mathcal{Q}_p(1/\nu_0)$ and $\mathcal{P}_p(\nu_0)^\top = \nu_0^2\mathcal{P}_p(1/\nu_0)$ for $\nu_0 \neq 0$, below we only discuss how to solve the linear system $\mathcal{P}_p(\nu_0)\mathbf{v} = \mathbf{d}$ when an iterative solver is applied to (31).

Theorem 6. *With $\Lambda_\ell, \widetilde{\Lambda}_\ell, \ell = 1, 2, 3$ defined in (37a)–(37c) and T in (38) and $P_0(\tau)$ in (20), the linear system*

$$\mathcal{P}_p(\nu_0)\mathbf{v} = \mathbf{d} \tag{41}$$

can be transformed into

$$\begin{aligned}&\left((\nu_0 \pm 1)^2\omega^2\alpha I \mp \nu_0 I_3 \otimes (P_{0\Lambda}(\nu_0^{-1})P_{0\Lambda}(\bar{\nu}_0)^*)\right)\widetilde{\mathbf{v}}\\ &= 4\left(I \mp \nu_0(\nu_0 \pm 1)^{-2}\omega^{-2}\alpha^{-1}P_{0\Lambda}(\bar{\nu}_0)^*P_{0\Lambda}(\nu_0^{-1})\right)(I_3 \otimes T)^*\,\mathbf{d},\end{aligned} \tag{42}$$

where $\widetilde{\mathbf{v}} = (I_3 \otimes T)^*\,\mathbf{v}$ and

$$P_{0\Lambda}(\nu) := [(\nu\mp 1)\widetilde{\Lambda}_1 + (\nu\pm 1)\Lambda_1 \quad (\nu\mp 1)\widetilde{\Lambda}_2 + (\nu\pm 1)\Lambda_2 \quad (\nu\mp 1)\widetilde{\Lambda}_3 + (\nu\pm 1)\Lambda_3]. \tag{43}$$

Proof. With (32a), (39) and (40), it holds that

$$\mathcal{P}_p(\nu_0) = \frac{1}{4}(\nu_0 \pm 1)^2\left[\omega^2\alpha I - I_3 \otimes (P_0(-\tau_0)P_0(\tau_0)^\top) + P_0(\tau_0)^\top P_0(-\tau_0)\right],$$

which implies that the linear system (41) is equivalent to

$$(\nu_0 \pm 1)^2\left(\omega^2\alpha I - I_3 \otimes (P_0(-\tau_0)P_0(\tau_0)^\top)\right)\mathbf{v} = 4\mathbf{d} - (\nu_0 \pm 1)^2 P_0(\tau_0)^\top P_0(-\tau_0)\mathbf{v}. \tag{44}$$

Multiplying both sides of (41) by $4P_0(\tau_0)^\top P_0(-\tau_0)$ and using (21), we have

$$(\nu_0 \pm 1)^2\omega^2\alpha P_0(\tau_0)^\top P_0(-\tau_0)\mathbf{v} = 4P_0(\tau_0)^\top P_0(-\tau_0)\mathbf{d},$$

thus (44) becomes

$$\begin{aligned}&\left\{(\nu_0 \pm 1)^2\omega^2\alpha I - I_3 \otimes \left[((\nu_0 \pm 1)P_0(-\tau_0))((\nu_0 \pm 1)P_0(\tau_0))^\top\right]\right\}\mathbf{v}\\ &= 4\left\{I - (\nu_0 \pm 1)^{-2}\omega^{-2}\alpha^{-1}((\nu_0 \pm 1)P_0(\tau_0))^\top((\nu_0 \pm 1)P_0(-\tau_0))\right\}\mathbf{d}.\end{aligned} \tag{45}$$

Recalling the eigen-decompositions (36) and $P_{0\Lambda}(\nu)$ in (43), we have

$$(\nu_0 \pm 1)P_0(-\tau_0) = (\nu_0 \pm 1)P_0\left(-\frac{\nu_0 \mp 1}{\nu_0 \pm 1}\right) = \pm\nu_0(\nu_0^{-1} \pm 1)P_0\left(\frac{\nu_0^{-1} \mp 1}{\nu_0^{-1} \pm 1}\right)$$
$$= \pm\nu_0 T P_{0\Lambda}(\nu_0^{-1})(I_3 \otimes T)^*, \quad \nu_0 \neq 0. \tag{46}$$

On the other hand, since $\widetilde{C}_\ell$ and $C_\ell, \ell = 1, 2, 3$, are real matrices, we have

$$((\nu_0 \pm 1)P_0(\tau_0))^\top = ((\bar{\nu}_0 \pm 1)P_0(\bar{\tau}_0))^* = (I_3 \otimes T)P_{0\Lambda}(\bar{\tau}_0)T^*. \tag{47}$$

Substituting (46) and (47) into (45), it is easy to see the solution $\mathbf{v}$ in (45) can be retrieved from (42). □

Remark 2. *Thanks to Theorem 6, multiplying a column vector by $\mathcal{P}_p(\nu_0)^{-1}$ and $\mathcal{P}_p(\nu_0)^{-\top}$ is essentially reduced to $T\mathbf{q}$ and $T^*\mathbf{p}$, where $\mathbf{q}$ and $\mathbf{p}$ are some intermediate vectors. Notably, $T\mathbf{q}$ and $T^*\mathbf{p}$ can be computed via the backward and forward FFTs, respectively, details of which can be found in Algorithm 1 and 2 in [6], respectively. This is one remarkable benefit brought by YS. In passing, $I_3 \otimes (P_{0\Lambda}(\nu_0^{-1})P_{0\Lambda}(\bar{\nu}_0)^*)$ in (42), after a suitable permutation of rows and columns, becomes the direct sum of n matrices of size 3-by-3.*

5. Numerical Results

5.1. Problem settings

In our numerical experiments, we only consider the 3D PC with the BCC lattice specified in the beginning of Sec. 2. In the primitive cell of the BCC lattice, as shown in Fig. 2(a), there are two different media, separated by the interface $\{\mathbf{x} \in \mathbb{R}^3 : g(\mathbf{x}) = 1.1\}$, with $g(\mathbf{x}) = g(x, y, z)$ defined by [15]

$$g(\mathbf{x}) = \sin(2\pi x/\tilde{a})\cos(2\pi y/\tilde{a}) + \sin(2\pi y/\tilde{a})\cos(2\pi z/\tilde{a}) + \sin(2\pi z/\tilde{a})\cos(2\pi x/\tilde{a}),$$

with $\tilde{a}$ being the lattice constant. Here, $\tilde{a}$ is simply set to 1. The permittivity of the media inside the single gyroid region $\{\mathbf{x} \in \mathbb{R}^3 : g(\mathbf{x}) > 1.1\}$ is $\varepsilon_1(\omega)$, while the rest space of the primitive cell is just air. That is, in our problem,

$$\varepsilon(\mathbf{x}, \omega) = \begin{cases} \varepsilon_1(\omega), & \text{if } g(\mathbf{x}) > 1.1 \\ \varepsilon_0, & \text{otherwise} \end{cases}. \tag{48}$$

We will separately consider a non-dispersive model [15]

$$\varepsilon_1(\omega) = 16\varepsilon_0, \quad \varepsilon_0 = 1, \tag{49a}$$

and a dispersive model called Drude model [4, 8, 16]

$$\varepsilon_1(\omega) = \left(1 - \frac{\omega_p^2}{\omega(\omega - \imath\Gamma_p)}\right)\varepsilon_0, \quad \varepsilon_0 = 1, \tag{49b}$$

with $\omega_p = 9$ and $\Gamma_p = 0.054$ [4].

With reciprocal lattice vectors $\{\mathbf{b}_\ell\}_{\ell=1}^3$ of this lattice which satisfy $\mathbf{b}_\ell \cdot \mathbf{a}_{\ell'} = \delta_{\ell'}^{\ell}$ for $\ell, \ell' = 1, 2, 3$, we can define the FBZ of this lattice. Usually, for the BCC lattice, it suffices to consider the irreducible FBZ, which, as shown in Fig. 2(b), is the tetrahedron with four vertices $\Gamma = [0, 0, 0]^\top$, $N = \mathbf{b}_3/2$, $H = (\mathbf{b}_1 - \mathbf{b}_2 + \mathbf{b}_3)/2$ and $P = (\mathbf{b}_1 + \mathbf{b}_2 + \mathbf{b}_3)/4$ [19]. Furthermore, like the famous Gauss map in differential geometry, we can map the wave vector $\mathbf{k}$ whose end point lies within $\triangle PHN$ to the unit sphere, resulting in a spherical $\triangle \widetilde{P}\widetilde{H}\widetilde{N}$, illustrated in Fig. 2(c), where $\widetilde{N} = N/\|N\|, \widetilde{H} = H/\|H\|$ and $\widetilde{P} = P/\|P\|$. We will take the normal vectors of this spherical $\triangle \widetilde{P}\widetilde{H}\widetilde{N}$ as those $\tilde{\mathbf{k}}$'s in (6).

All computations below are carried out on the Matlab R2019a platform. Unless otherwise stated, the dimension of the QEP (18) below is set to $3 \times 120^3 = 5,184,000$, which is larger than 10^6, and the stopping criterion of the G⊤SHIRA algorithm is set to 10^{-10}. Moreover, we require that Algorithm 1 be restarted [9] every 30 iterations until all target eigenpairs converge.

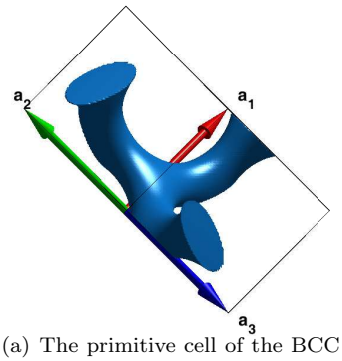

(a) The primitive cell of the BCC lattice with a gyroid region inside.

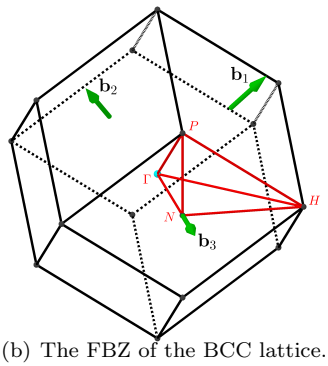

(b) The FBZ of the BCC lattice.

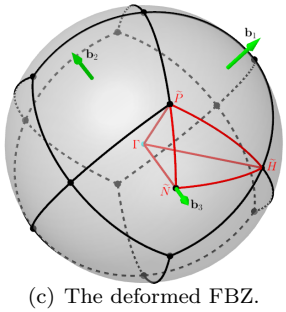

(c) The deformed FBZ.

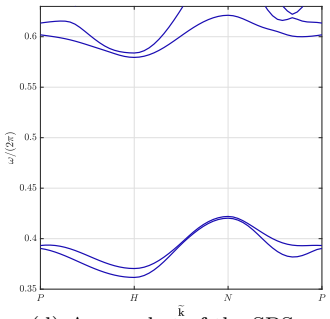

(d) A snapshot of the SBS.

Figure 2: (a) Illustration of the BCC lattice and the gyroid region. (b) The solid polyhedron with black edges denote the FBZ of the BCC lattice, and green arrows denote reciprocal lattice vectors $\mathbf{b}_1$, $\mathbf{b}_2$ and $\mathbf{b}_3$. (c) The region enclosed by red line denotes the corresponding deformed irreducible FBZ. (d) Illustration of SBS of the 3D non-dispersive PC which has a bandgap, with ε in (49a).

5.2. The two-stage strategy to solve (31)

There are many iterative methods to solve large sparse linear systems [18], and it is unlikely to tell in advance which is best for a particular job. Here, we just practically compare the performance of some commonly used linear solvers such as **tfqmr**, **bicgstab**, **bicgstabl** and **gmres**, with and without the preconditioner (40), when solving (31) to the tolerance 10^{-12} for the dispersive model (49b) with $\omega = 0.4\pi, \nu_0 = \exp(\imath 0.1\pi)$. As shown in Fig. 3, the preconditioner (40) is indispensable, comparing the behavior of **bicgstabl** with the preconditioner (40) and that without the preconditioner.

From Fig. 3, we find that **tfqmr**, **bicgstab** and **bicgstabl**, aided with the preconditioner (40), are nearly equally efficient. They can make the residual of the linear systems (31) drop to a plateau at almost the same speed, except that **tfqmr** suffers from the stagnation more frequently during the iterative process. Unfortunately, none of them is eventually able to maintain the desired residual norm as the iteration continues. By contrast, it takes more iterations to reach the target tolerance if **gmres** aided with the preconditioner (40) is utilized, but no oscillating residual norm is observed. In other words, **gmres** is quite stable.

These preliminary investigations suggest us combining the advantages of **bicgstabl** and **gmres** to devise a two-stage strategy to solve (31). Specifically, we first call **bicgstabl** to solve the linear systems (31), with the tolerance set to 10^{-9}, then we take the approximate solution from the former as the initial vector for **gmres**, and take the approximate solution from **gmres** with a tighter tolerance 10^{-12}, as the final solution to (31). As witnessed in Fig. 3, **bicgstabl** plus **gmres** is not plagued with the stagnation and especially can maintain the desired residual norm robustly. That is to say, this strategy works quite well.

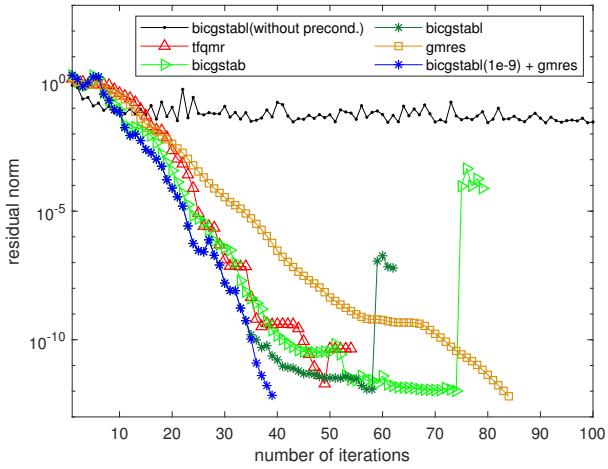

Figure 3: The convergence behavior of some iterative solvers when solving (31).

5.3. The CBS of a 3D non-dispersive PC

To verify our method, here we compute the CBS of a 3D non-dispersive PC whose ε is specified in (48) and (49a), with lattice parameters specified in the beginning of Sec. 5.1. In this case, we can routinely compute its SBS, from which the bandgap information is directly accessed. Furthermore, for the BCC lattice, it suffices to consider the irreducible FBZ illustrated in Fig. 2(b) to compute the SBS. Recall that, by saying that $[\omega_1, \omega_2] \subset \mathbb{R}^+$ is a bandgap of a PC, we mean for any $\mathbf{k} \in \mathbb{R}^3$ no $\omega \in [\omega_1, \omega_2]$ satisfies (2) or (5). As is shown in Fig. 2(d), the SBS analysis of this 3D PC clearly indicates the existence of the bandgap.

It is anticipated that by solving eigenvalues τ which are closest to or on the imaginary axis of the GQEP (23) for ω outside the bandgap, we can obtain at least one $-\imath\tau\tilde{\mathbf{k}}$ with $\tau \in \imath\mathbb{R}$ that coincides with the $\mathbf{k}$ used in the SBS calculation to produce the same ω. This partially explains why we only consider $\tilde{\mathbf{k}}$'s within the spherical $\triangle\widetilde{P}\widetilde{H}\widetilde{N}$. In return, via computing the CBS of this 3D PC we can obtain the same bandgap, because the GQEP (23) has no purely imaginary eigenvalues for ω within the bandgap.

Specifically, for this model, we first set $\tilde{\mathbf{k}}$ to $\widetilde{P}$ and generate 112 samples of ω's that are evenly distributed in $[0.6\pi, 1.3\pi]$. For each given ω, we compute 6 eigenvalues $\{\nu_i\}_{i=1}^6$ nearest or on $\mathbb{T}$ of the $\top$-PQEP (25a) with $\Im\nu_i \geq 0$. After transforming $\{\nu_i\}_{i=1}^6$ back to eigenvalues $\{\lambda_i\}_{i=1}^{12}$ of the QEP (18), which are shown in Fig. 4, it is estimated that no $\omega \in [0.838\pi, 1.3\pi]$ correspond to a $\mathbf{k} = \lambda\tilde{\mathbf{k}} \in \mathbb{R}^3$. To obtain more accurate bounds of bandgaps of this model, then we sample more $\tilde{\mathbf{k}}$'s within the spherical $\triangle\widetilde{P}\widetilde{H}\widetilde{N}$. For each $\tilde{\mathbf{k}}$ and ω mentioned above, we similarly compute 6 eigenvalues $\{\nu_i\}_{i=1}^6$ of (25a) nearest or on $\mathbb{T}$ with $\Im\nu_i \geq 0$, and transform them back to $\{\lambda_i\}_{i=1}^{12}$ of (18). To provide a synthetic vision of all data prepared for this model, we only choose two $\Im\lambda$'s whose moduli are the minimal among the imaginary part of $\{\lambda_i\}_{i=1}^{12}$ computed for each $\tilde{\mathbf{k}}$ and ω, and show a 3D plot of the surface of $\Im\lambda$ versus $\tilde{\mathbf{k}}$ and ω in Fig. 5(a). Owing to the real ε, there are two surfaces in Fig. 5(a) which are symmetric about a plane $\Im\lambda = 0$. More importantly, it is completely hollow between these two surfaces, which is the signature of the bandgap.

Furthermore, the vertical view of Fig. 5(a) is shown in Fig. 5(b). Here we regard an eigenvalue λ as a real number if $|\Im\lambda| \leq 10^{-6}$. Then we can draw two red lines attached to the ω-axis which denote the lower and upper bound of the bandgap inferred from the CBS computations. As expected, the bandgap shown in Fig. 5(b) is in good agreement with that from the SBS analysis in Fig. 2(d).

5.4. The efficiency of the preconditioner (40)

In each iteration of the G$\top$SHIRA algorithm, we adopt the two-stage strategy mentioned in Sec. 5.2, i.e., **bicgstabl** followed up with **gmres** and both armed with the preconditioner (40), to solve two linear systems in (31). Here, we use the total iteration number (TIN) of these two preconditioned solvers to characterize the efficiency of the preconditioner (40). We test our preconditioner separately on the non-dispersive and dispersive model, with various matrix dimensions $3n$ and shifts $\nu_0 = \exp(\imath 2\pi\theta) \in \mathbb{T}$, where $\theta \in (0, 1)$.

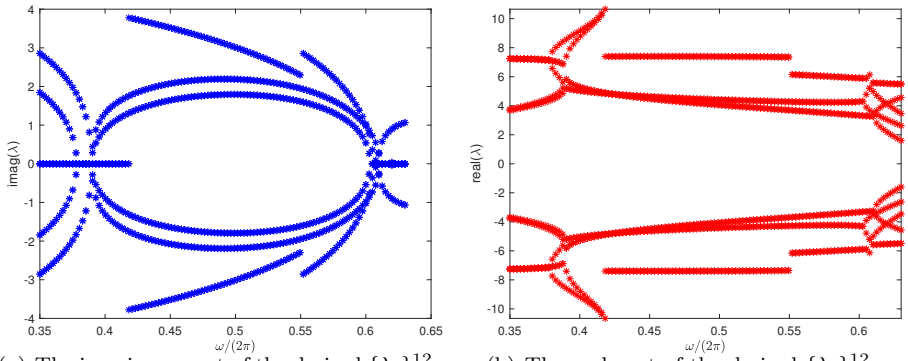

(a) The imaginary part of the desired $\{\lambda_i\}_{i=1}^{12}$. (b) The real part of the desired $\{\lambda_i\}_{i=1}^{12}$.

Figure 4: The (a) imaginary part and (b) real part of $\{\lambda_i\}_{i=1}^{12}$ which are closest to $\lambda_0 = 1$ for $\omega \in [0.7\pi, 1.3\pi]$, given $\tilde{\mathbf{k}} = \widetilde{P}$.

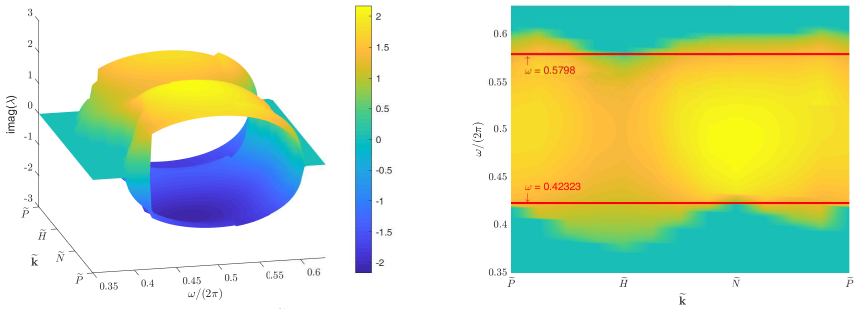

(a) Surfaces of $\Im\lambda$ *vs.* $\tilde{\mathbf{k}}$ and ω. (b) The estimate of bounds of the bandgap.

Figure 5: The bandgap estimated from CBS computations.

We first discuss the results in Fig. 6(a) and Fig. 6(b) of the dispersive model (49b). In Fig. 6(a), we set $\omega = 0.2\pi$ in (18) and (49b), and the dimension of the linear system is $3n = 3n_1^3$ with $n_1 = 30:10:120$, which ranges from $81,000$ to $5,184,000$. We can see that when θ is away from 0 and 1, the TIN for solving (31) falls between 40 and 65, which shows little variance compared with the matrix dimension. In other words, the TIN is almost independent of the matrix dimension and the shift ν_0. Amazingly, even the size of the linear system is of the order of magnitude of five million, we can still reach the tolerance of 10^{-12} with TIN no more than 65. On the other hand, when θ is very near 1, which is not shown in Fig. 6(a), the TIN is supposed to increase a lot, since the $\top$-PQEP (25a) and the linear systems (31) become singular when $\theta = 1$ exactly.

In Fig. 6(b), we set the matrix dimension to $5,184,000$ and examine the performance of our preconditioned iterative solver applied to (31) for different $\omega \in [0.2\pi, 0.6\pi]$ as well as $\theta \in (0, 1)$. As shown in Fig. 6(b), we can see that the

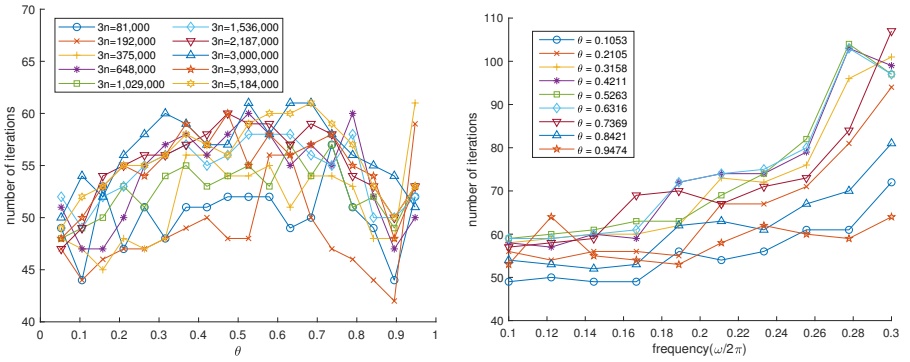

(a) TIN *vs.* matrix dimension with $\omega = 0.2\pi$. (b) TIN *vs.* θ with matrix dimension $5,184,000$.

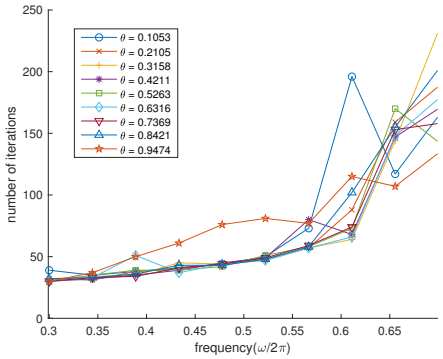

(c) TIN *vs.* θ with matrix dimension $5,184,000$.

Figure 6: TIN of solving (31) with tolerance 10^{-12} for (a)-(b) the dispersive model and (c) the non-dispersive model.

TIN ranges from 50 to 110, which certainly depends on ω but is less sensitive to θ. In other words, without more information of the underlying model, there is not much sense to choose a particular shift ν_0 as long as θ is not near 0 or 1. To sum up, the TINs shown in Fig. 6(a) and Fig. 6(b) for solving linear systems (31) are remarkably small in view of the dimension being as large as 5.2 million, which implies that the preconditioner (40) is quite effective for the dispersive model for any shift ν_0 away from 1 and various ω of interest.

Next, we discuss the results of the non-dispersive model (49a). In Fig. 6(c), similarly, the matrix dimension being set to $5,184,000$, we examine how the TIN for (31) changes with $\omega \in [0.6\pi, 1.4\pi]$ for various θ. We can see that on the whole the TIN shown in Fig. 6(c) increases from 30 to 250 as ω increases. This is because in this case, the larger ω is, the greater disparity between $\mathcal{P}_p(\mu_0)$ and $\mathcal{Q}_p(\mu_0)$ is. Hence, the efficiency of the preconditioner (40) is negatively correlated with ω, which agrees with the trend of curves in Fig. 6(c). Anyhow, all the TINs are impressively small compared with the matrix dimension, which indicates that the preconditioner (40) is also very effective for the non-dispersive

k	P	$(3P+H)/4$	$(P+H)/2$	$(P+3H)/4$	H	$(3H+N)/4$
ANR	3.7	2.4	2.5	2.8	3.5	2.5
k	$(H+N)/2$	$(H+3N)/4$	$(N+P)/2$	$(3N+P)/4$	N	$(N+3P)/4$
ANR	2.4	2.8	2	2.8	2.3	2

Table 1: The average number of restarts (ANR) of G⊤SHIRA for the non-dispersive model.

model for any shift ν_0 away from 1 and various ω of interest.

5.5. The efficiency of the G⊤SHIRA algorithm

In Sec. 5.3, to compute the 3D non-dispersive PC, the G⊤SHIRA algorithm is the workhorse, and the shift is always set to $\eta_0 = \nu_0 + 1/\nu_0 = 1\imath + 1/(1\imath) = 0$. Here we report its performance. Since Algorithm 1 is required be restarted every 30 iterations, the most straighforward characterization of the efficiency of the G⊤SHIRA algorithm is the number of restarts. Recall that to obtain the surfaces in Fig. 5(a) we sample 112 different ω's in $[0.6\pi, 1.3\pi]$ for a given $\tilde{\mathbf{k}}$. For each $\tilde{\mathbf{k}}$, we average the corresponding 112 numbers of restarts of the G⊤SHIRA algorithm and show the results in Table. 1, where $\mathbf{k}$ instead of $\tilde{\mathbf{k}} = \mathbf{k}/\|\mathbf{k}\|$ is provided. Clearly, the average number of restarts is no more than 4 for each $\tilde{\mathbf{k}}$.

In addition, for the dispersive model (49b), we have also carried out several illustrative calculations. Specifically, we set $\omega = 0.2\pi$ in (49b), and only calculate two eigenvalues of the ⊤-PQEP (25a) nearest to the shift $\nu_0 = \exp(\imath 2\pi\theta)$ with $\theta = 0.1, 0.2, 0.3$ and 0.4, respectively, as well as the corresponding eignvectors. We find that the number of restarts of the G⊤SHIRA algorithm is just 3 for these shifts ν_0 to fully resolve the desired eigenvalues $\pm(0.0542 + \imath 0.1111)$ and $\pm(0.0536 - \imath 0.1107)$ of the ⊤-PQEP (25a).

In summary, all the numbers of restarts for both the non-dispersive and the dispersive models are tiny, considering the size of the pair $(\mathcal{K}, \mathcal{N})$, which means the G⊤SHIRA algorithm is highly efficient for our problem.

6. Conclusion

In this work, in conjunction of YS to discretize the constrained QOP (6) derived from source-free MEQs (5), we propose a fast structure-preserving algorithm to compute CBSs of 3D dispersive and non-dispersive *isotropic* PCs, with not only the real but also the complex permittivity $\varepsilon(\omega)$. Although in this article only 3D PCs with the BCC lattice are expounded, our method can be easily adapted for those with other Bravais lattices.

As is demonstrated in this work, YS indeed brings in several benefits for CBS computation of 3D PCs, which is similar to case of SBS computations of 3D non-dispersive PCs. The validity of the discretized divergence-free condition (19) is a natural consequence of YS. The explicit eigen-decompositions presented in Theorem 4 and 5 of components of discretized $\tilde{\mathbf{k}}\times$ and $\nabla\times$ operators profit from YS, too. Grounded on these eigen-decompositions, we propose the FFT-based preconditioning techniques to significantly accelerate the convergence of

the inner iterations of the G⊤SHIRA algorithm. Additionally, the efficiency of our preconditioners is almost independent of the dimension of the linear system.

In a nutshell, our task in this work comes down to solving several eigenvalues of the resulting GQEP (23) which are closest to or on the imaginary axis but away from the origin. To this end, we carry forward the guiding principle used in our recent work [10]. That is, the GQEP and ⊤-PQEP can be mapped to one another via the Cayley transformation (24), at the cost of addition of a few matrices. Since we have a well-established computational framework for the ⊤-PQEP, which is outlined in Sec. 3, then via the Cayley transformation, we can naturally apply this framework to the GQEP. As shown in Sec. 5.5, the number of outer iterations of the G⊤SHIRA algorithm remains remarkably small for both the non-dispersive and the dispersive model, even though the dimension of the GQEP rises up to five million. This is attributed to a series of spectral transformations described in Sec. 3.1 which greatly widen the distance between the desired eigenvalues and the unwanted ones. In consequence, the efficiency of CBS computations of 3D PCs has been greatly improved.

To sum up, our structure-preserving method looks very promising for calculating CBSs of 3D PCs. Currently, generalization of our structure-preserving method to calculating CBSs of 3D *anisotropic* PCs and *bi-isotropic* and *bian-isotropic* metamaterial crystals is under consideration.

Acknowledgements

The authors were partially supported by both ST Yau Centers in Chiao Tung University and Southeast University. T.-M. Huang was partially supported by the Ministry of Science and Technology (MoST) 105-2115-M-003-009-MY3, National Center for Theoretical Sciences (NCTS) in Taiwan. T. Li was supported in parts by the NSFC 11471074. W.-W. Lin was partially supported by MoST 106-2628-M-009-004-. H. Tian was supported by MoST 107-2811-M-009-002-.

AppendixA. Some formulas for the simple cubic lattice

Corresponding to (15a)–(15c), we have very simple expressions of $C_\ell, \widetilde{C}_\ell, \ell = 1, 2, 3$ for the simple cubic lattice as follows,

$$C_1 = I_{n_3} \otimes I_{n_2} \otimes (K_1(n_1) - I_{n_1})/\delta_x,\ \widetilde{C}_1 = \widetilde{k}_1 I_{n_3} \otimes I_{n_2} \otimes (K_1(n_1) + I_{n_1})/2, \quad \text{(A.1a)}$$

$$C_2 = I_{n_3} \otimes (K_1(n_2) - I_{n_2}) \otimes I_{n_1}/\delta_y,\ \widetilde{C}_2 = \widetilde{k}_2 I_{n_3} \otimes (K_1(n_2) + I_{n_2}) \otimes I_{n_1}/2, \quad \text{(A.1b)}$$

$$C_3 = (K_1(n_3) - I_{n_3}) \otimes I_{n_2} \otimes I_{n_1}/\delta_z,\ \widetilde{C}_3 = \widetilde{k}_3 (K_1(n_3) + I_{n_3}) \otimes I_{n_2} \otimes I_{n_1}/2, \quad \text{(A.1c)}$$

where $K_1(m) := \begin{bmatrix} 0 & I_{m-1} \\ 1 & 0 \end{bmatrix}_{m \times m}$, $m \in \mathbb{N}$.

Corresponding to Theorem 5, here, we only need to consider the eigen-decomposition of the circulant matrix $K_1(m)$, which is quite trivial.

Theorem 7. *Eigen-decompositions of* C_ℓ *and* $\widetilde{C}_\ell, \ell = 1, 2, 3$ *in* (A.1) *are*

$$C_\ell = T\Lambda_\ell T^*, \quad \widetilde{C}_\ell = T\widetilde{\Lambda}_\ell T^*, \quad \ell = 1, 2, 3, \tag{A.2}$$

respectively, where

$$\Lambda_1 = (I_{n_3} \otimes I_{n_2} \otimes \Lambda_{n_1} - I_n)/\delta_x, \ \widetilde{\Lambda}_1 = \widetilde{k}_1(I_{n_3} \otimes I_{n_2} \otimes \Lambda_{n_1} + I_n)/2, \tag{A.3}$$

$$\Lambda_2 = (I_{n_3} \otimes \Lambda_{n_2} \otimes I_{n_1} - I_n)/\delta_y, \ \widetilde{\Lambda}_2 = \widetilde{k}_2(I_{n_3} \otimes \Lambda_{n_2} \otimes I_{n_1} + I_n)/2, \tag{A.4}$$

$$\Lambda_3 = (\Lambda_{n_3} \otimes I_{n_2} \otimes I_{n_1} - I_n)/\delta_z, \ \widetilde{\Lambda}_3 = \widetilde{k}_3(\Lambda_{n_3} \otimes I_{n_2} \otimes I_{n_1} + I_n)/2, \tag{A.5}$$

$$\Lambda_{n_\ell} = \mathbf{diag}\left(\exp(\imath 2\pi[0\!:\!n_\ell - 1]^\top/n_\ell)\right), \quad \ell = 1, 2, 3, \tag{A.6}$$

and $T = F_{n_3} \otimes F_{n_2} \otimes F_{n_1}$ *with* F_m *being the discrete Fourier transform matrix* $[F_m]_{p,q} = m^{-1/2}\exp(\imath 2\pi(p-1)(q-1)/m)$, $1 \le p, q \le m$, $m \in \mathbb{N}$.

References

[1] R.-L. Chern, H.-E. Hsieh, T.-M. Huang, W.-W. Lin, and W. Wang. Singular value decompositions for single-curl operators in three-dimensional Maxwell's equations for complex media. *SIAM J. Matrix Anal. Appl.*, 36:203–224, 2015.

[2] M. Davanco, Y. Urzhumov, and G. Shvets. The complex Bloch bands of a 2D plasmonic crystal displaying isotropic negative refraction. *Opt. Express*, 15(15):9681, 2007.

[3] C. Engström and M. Richter. On the spectrum of an operator pencil with applications to wave propagation in periodic and frequency dependent materials. *SIAM J. Appl. Math.*, 70(1):231–247, 2009.

[4] C. Fietz, Y. Urzhumov, and G. Shvets. Complex k band diagrams of 3D metamaterial/photonic crystals. *Opt. Express*, 19(20):19027, 2011.

[5] Y.-C. Hsue, A. J. Freeman, and B.-Y. Gu. Extended plane-wave expansion method in three-dimensional anisotropic photonic crystals. *Phys. Rev. B*, 72(19), 2005.

[6] T.-M. Huang, H.-E. Hsieh, W.-W. Lin, and W. Wang. Eigendecomposition of the discrete double-curl operator with application to fast eigensolver for three dimensional photonic crystals. *SIAM J. Matrix Anal. Appl.*, 34:369–391, 2013.

[7] T.-M. Huang, T. Li, W.-D. Li, J.-W. Lin, W.-W. Lin, and H. Tian. Solving three dimensional Maxwell eigenvalue problem with fourteen Bravais lattices. Technical report, arXiv:1806.10782, 2018.

[8] T.-M. Huang, W.-W. Lin, and V. Mehrmann. A Newton-type method with nonequivalence deflation for nonlinear eigenvalue problems arising in photonic crystal modeling. *SIAM J. Sci. Comput.*, 38:B191–B218, 2016.

[9] T.-M. Huang, W.-W. Lin, and J. Qian. Structure-preserving algorithms for palindromic quadratic eigenvalue problems arising from vibration on fast trains. *SIAM J. Matrix Anal. Appl.*, 30:1566–1592, 2008.

[10] T.-M. Huang, W.-W. Lin, H. Tian, and G.-H. Chen. Computing the full spectrum of large sparse palindromic quadratic eigenvalue problems arising from surface Green's function calculations. *J. Comput. Phys.*, 356:340–355, 2018.

[11] T.-M. Huang, W.-W. Lin, and W. Wang. A hybrid Jacobi-Davidson method for interior cluster eigenvalues with large null-space in three dimensional lossless Drude dispersive metallic photonic crystals. *Comput. Phys. Commun.*, 207:221–231, 2016.

[12] C. Kittel. *Introduction to solid state physics*. Wiley, New York, NY, 2005.

[13] O. Leminger. Wave-vector diagrams for two-dimensional photonic crystals. *Opt. Quant. Electron.*, 34(5-6):435–443, 2002.

[14] W.-W. Lin. A new method for computing the closed-loop eigenvalues of a discrete-time algebraic Riccatic equation. *Linear Algebra Appl.*, 96:157–180, 1987.

[15] L. Lu, L. Fu, J. D Joannopoulos, and M. Soljačić. Weyl points and line nodes in gyroid photonic crystals. *Nat. Photonics*, 7:294–299, 2013.

[16] M. Luo and Q. H. Liu. Three-dimensional dispersive metallic photonic crystals with a bandgap and a high cutoff frequency. *J. Opti. Soc. Amer. A*, 27(8):1878–1884, 2010.

[17] V. Mehrmann and D. Watkins. Structure-preserving methods for computing eigenpairs of large sparse skew-Hamiltonian/Hamiltonian pencils. *SIAM J. Sci. Comput.*, 22:1905–1925, 2001.

[18] Y. Saad. *Iterative methods for sparse linear systems*. PWS Publishing Company, Boston, MA, 1996.

[19] W. Setyawan and S. Curtarolo. High-throughput electronic band structure calculations: Challenges and tools. *Comput. Mater. Sci.*, 49:299–312, 2010.

[20] A. J. Ward, J. B. Pendry, and W. J. Stewart. Photonic dispersion surfaces. *J. Phys. Condens. Matter*, 7(10):2217–2224, 1995.

[21] W. S. Weiglhofer and A. Lakhtakia. *Introduction to Complex Mediums for Optics and Electromagnetics*. SPIE, Washington, DC, 2003.

[22] K. Yee. Numerical solution of initial boundary value problems involving Maxwell's equations in isotropic media. *IEEE Trans. Antennas and Propagation*, 14:302–307, 1966.